Polarix: Monitoring Multi-Component Liquids via Polarized Light

Juntao Zhou[1,4†],Longyuan Ge[1,4†],Yi-Chao Chen[1,4*],Qianfei Ren[1,4],Yijie Li[2*],Dian Ding[1,4*],Yida Wang[1,4],Hao Pan[1,4],Lili Qiu[3],Jiadi Yu[1],Lanqing Yang[1,4],Guangtao Xue[1,4]
[1]Shanghai Jiao Tong University, [2]Shanghai University of Finance and Economics, [3]University of Texas at Austin, [4]Shanghai Key Laboratory of Trusted Data Circulation and Governance, and Web3
{juntaozhou,gly2000,yichao,cordial.Daniel}@sjtu.edu.cn, liyijie@sufe.edu.cn,
{dingdian94, yidawang, panh09}@sjtu.edu.cn, lili@cs.utexas.edu, {jiadiyu,yanglanqing,gt_xue}@sjtu.edu.cn

Abstract

Optically active substances such as sugars and amino acids are critical quality indicators in biomanufacturing and food safety, yet they typically coexist as multi-component mixtures. Existing monitoring techniques either require expensive instruments (e.g., HPLC) with per-sample costs and turnaround times ill-suited for online control, or rely on optical methods that cannot resolve individual component concentrations from a mixture. We present Polarix, a training-free polarimetric platform built from $100 in hardware that exploits a fundamental physical property: the specific optical rotation of each optically active substance varies with temperature at a distinct, substance-dependent rate. By sweeping the sample temperature across a bounded 15°C window, Polarix transforms the underdetermined problem into a solvable system, mathematically disentangling each component's concentration. Its optical design improves robustness against real-world disturbances including turbidity, flow, and mechanical drift. We validate Polarix on three real-world tasks: amino-acid fermentation tracking, trace byproduct detection, and honey adulteration screening against rice syrup and HFCS-55. Polarix resolves individual component concentrations with a mean relative error of 12.1%.

CCS Concepts

• **Human-centered computing → Ubiquitous and mobile computing systems and tools**.

Keywords

Multi-component liquid sensing, Polarized light

† Authors contributed equally to this research. ∗ Corresponding authors.

This work is licensed under a Creative Commons Attribution-NonCommercial-NoDerivatives 4.0 International License.
MobiCom '26, Austin, TX, USA
© 2026 Copyright held by the owner/author(s).
ACM ISBN 979-8-4007-2505-0/2026/10
https://doi.org/10.1145/3795866.3844475

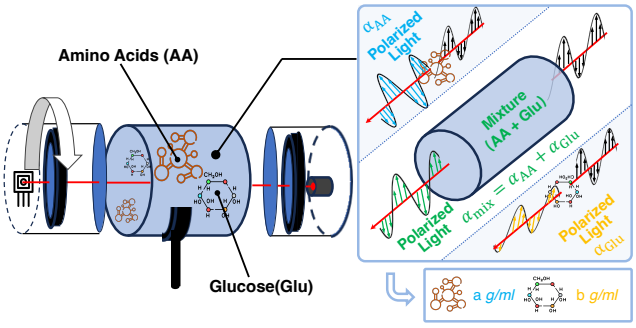


Figure 1: Polarix is a polarimetric sensing platform that resolves concentrations of multiple components (e.g., amino acids and glucose) in a mixed solution.

ACM Reference Format:
Juntao Zhou[1,4†],Longyuan Ge[1,4†],Yi-Chao Chen[1,4*],Qianfei Ren[1,4], Yijie Li[2*],Dian Ding[1,4*],Yida Wang[1,4],Hao Pan[1,4],Lili Qiu[3],Jiadi Yu[1], Lanqing Yang[1,4],Guangtao Xue[1,4]. 2026. Polarix: Monitoring Multi-Component Liquids via Polarized Light. In *The 32nd Annual International Conference on Mobile Computing and Networking (MobiCom '26), October 26–30, 2026, Austin, TX, USA.* ACM, New York, NY, USA, 16 pages. https://doi.org/10.1145/3795866.3844475

1 Introduction

Optically active substances such as amino acids, sugars, and organic acids serve as indispensable quality and process indicators across biomanufacturing, pharmaceuticals, and the food industry [1, 9, 71]. In practice, these substances rarely exist in isolation but form complex multi-component mixtures whose individual concentrations must be tracked simultaneously. A prominent example is large-scale microbial fermentation, the dominant route for producing essential amino acids such as lysine (global market: 1.26 billion USD in 2023 [14]), threonine, and alanine [39, 65]. During fermentation, the broth is a dynamic mixture of sugar substrates (e.g., glucose) and synthesized amino acid products. Maintaining the proper substrate balance is critical: depletion starves microbes [69], while excess promotes unwanted

byproducts that increase purification costs by 5–10% and reduce yields by up to 12% [17]. Beyond bioreactors, multi-component analysis is also essential in food authentication. Natural honey is certified by its native fructose-to-glucose ratio but is frequently adulterated with cheap syrups; recent surveillance found that 46% of honey sampled at EU borders and up to 10% of FDA-inspected U.S. imports were suspected non-compliant [4, 61, 67]. The need to monitor multiple optically active substances also arises in pharmaceutical quality control, clinical diagnostics, and environmental or bioprocess monitoring, where the concentrations of coexisting chiral molecules or metabolites must be verified against strict standards [31, 46, 58]. Across these scenarios, the core technical bottleneck remains determining the concentrations of individual components within multi-substance optically active liquids. Therefore, achieving precise, low-cost, and autonomous concentration tracking remains a critical unresolved sensing challenge.

Existing monitoring techniques remain fundamentally inadequate due to severe cost, latency, or physical resolution bottlenecks. The gold standards such as High-Performance Liquid Chromatography (HPLC) [12, 16, 19] and enzymatic assays [28, 30] deliver exceptional accuracy but require manual offline sampling, introducing hours of analytical latency that precludes real-time control. Inline biosensors bypass manual sampling but cost upwards of 1.5 million USD per system [18], target a single compound at a time, and cannot track the dynamic emergence of byproducts. Inline near-infrared (NIR) spectroscopy [34] reduces latency but demands equipment priced between 30,000 and 50,000 USD and relies on environment-specific chemometric models (e.g., PLS or neural networks) that fail to generalize across deployment scenarios. Moreover, the high per-unit cost of these inline instruments limits dense, per-vessel deployment, so continuous coverage is typically confined to few measurement points. Recent advances in ubiquitous liquid sensing exploit RF [47], Wi-Fi [11], millimeter-wave [7, 35], acoustic [55], vibration [21], and multi-wavelength optical absorption [20, 26, 37] signals. These modalities inherently measure macroscopic bulk properties such as dielectric constant or bulk absorption, which conflate contributions from structurally similar molecules and cannot decouple individual concentrations. Polarimetry is particularly sensitive to optically active substances [33, 58], yet traditional single-wavelength polarimeters face a fundamental physical barrier: the optical rotation of a mixture is the strict linear superposition of the rotations from each constituent [60]. Measuring an N-component mixture at a fixed temperature yields only one aggregate rotation value against N unknown concentrations, a severely underdetermined system with no unique solution [8]. A low-cost, training-free mechanism capable of multi-substance quantification in real-world liquids therefore remains an open problem.

To address this limitation, we introduce Polarix, a polarimetric sensing platform that exploits a critical physical phenomenon: different optically active substances exhibit distinctly different sensitivities in their specific optical rotation to temperature variations [13, 66]. For instance, glucose retains positive specific rotation, decreasing slightly with temperature, whereas fructose increases toward less-negative values via its complex mutarotation equilibrium, and each amino acid carries its own unique temperature response. By sweeping the sample temperature across a small 15°C window, Polarix transforms the inherently underdetermined static measurement into a solvable system of M equations in N unknowns, where the coefficient matrix has full column rank for substances with sufficiently distinct temperature responses [42]. To our knowledge, Polarix is the first system to leverage these differential temperature-dependent rotation rates to directly decouple and simultaneously quantify the individual concentrations of multiple solutes coexisting within a complex liquid mixture.

To further design a robust system that supports autonomous measurement, we faced several practical challenges and developed the corresponding solutions. First, in real-world deployments, target liquids are often turbid, colored, or dynamically flowing, conditions that corrupt traditional intensity-based [36] and half-shade [24] polarimeters. Polarix instead employs a continuously rotating analyzer and tracks the minimum-intensity phase of each rotation cycle, a quantity that depends on polarization angle and is robust to amplitude fluctuations by Malus' Law [5]. Second, stepper motors exhibit cumulative period jitter that progressively displaces the darkest-point position across rotation cycles. Polarix addresses this by attaching a physical light-blocking pilot strip to the analyzer, which creates a sharp and unambiguous intensity transient once per revolution to reset the cycle reference, reducing drift from a cumulative shift to a single-cycle noise term. Third, once the temperature-dependent specific-rotation curves are calibrated per substance in a one-time offline step, Polarix formulates concentration inference as a constrained least-squares problem solved with the L-BFGS-B optimizer without environment-specific training data.

We implemented Polarix into a compact prototype which features a localized heating tube that modulates the sampled volume across a 15°C window. Driven by a stepper motor, the pilot-equipped rotatable analyzer extracts the time-series light intensity, which our training-free algorithm translates into independent substance concentrations. We validate Polarix across three applications: dynamically tracking substrate-to-product conversion (glucose to lysine, threonine, and alanine) in operational bioreactors, detecting trace metabolic byproducts such as isoleucine that emerge during

fermentation, and authenticating honey by recovering the native fructose-to-glucose ratio under two industrial adulterants (rice syrup and HFCS-55). Across all evaluations, Polarix achieves an overall absolute relative difference (ARD) of 0.121, which falls within the 20% error tolerance commonly accepted for online screening and process monitoring [15], demonstrating effective autonomous monitoring of multiple substances in complex, optically active liquids. Moreover, with a per-unit cost of approximately 100 USD, Polarix is inexpensive enough to be deployed in individual vessels. Polarix targets known small-N mixtures ($N \leq 4$), a regime covering the dominant analytes monitored in amino-acid fermentation [57, 62], honey authentication [45, 68], and beverage and juice quality control [3, 27, 32], with each component present at a concentration above 0.005 g/mL.

Our contributions can be summarized as follows:

- We identify and exploit the differential temperature sensitivity of specific optical rotation across distinct optically active substances, transforming an underdetermined polarimetric system into a uniquely solvable one without any change in wavelength or path length.
- We design a minimum-intensity phase extraction method using a continuously rotating analyzer, achieving optical rotation measurement that is robust against turbidity, coloration, and flow-induced intensity fluctuations.
- We devise a physical pilot-strip mechanism on the rotating analyzer that eliminates cumulative motor drift, enabling stable measurements throughout multi-minute temperature sweeps.
- We develop a training-free, physics-grounded algorithm that directly infers multi-substance concentrations from a single temperature sweep.
- We implement a fully functional prototype costing near 100 USD and demonstrate an overall ARD of 0.121 across three diverse real-world sensing applications.

2 Related Work

2.1 Liquid Sensing

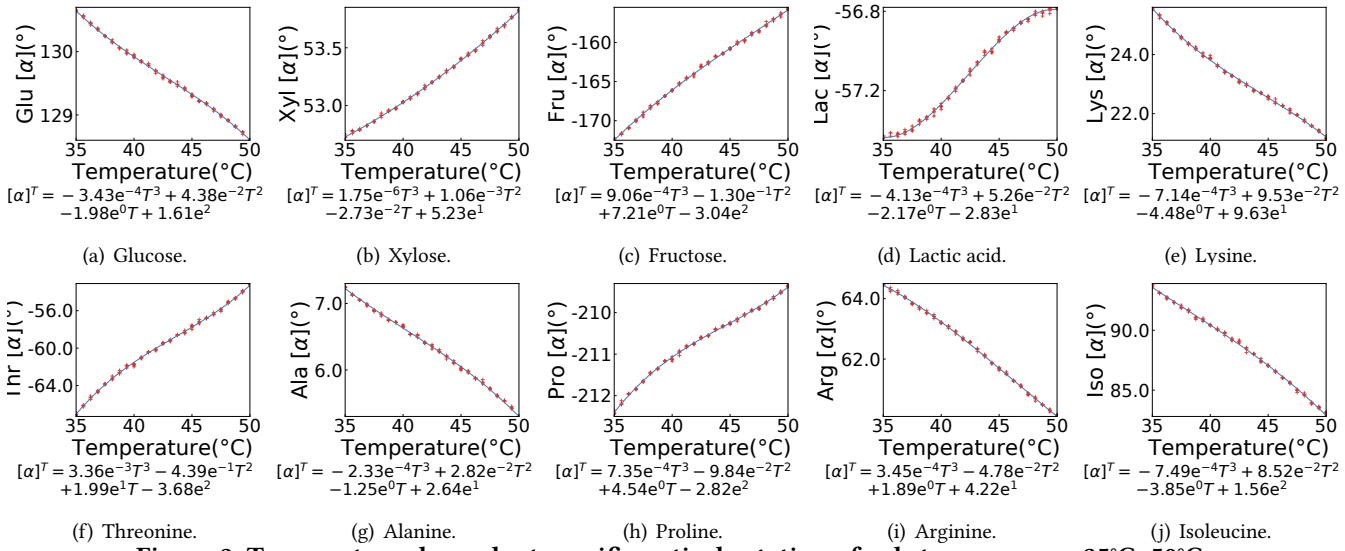
2.1.1 Wireless Signal-Based Liquid Sensing. A broad class of prior work exploits the way liquid dielectric or mechanical properties alter signal propagation, spanning RFID [63], UWB [10], WiFi [11], mmWave [7, 35], RF [47, 48], vibration [21], and acoustic [55] modalities. Despite this diversity, all such systems sense bulk properties of the mixture as a whole and cannot resolve individual component concentrations. Dispersive wireless signals further suffer from multipath interference and environmental variability, requiring per-deployment calibration or environment-specific machine learning models with poor cross-scenario generalization.

Table 1: Comparison of Liquid Sensing Systems

System	Sensing Modality	Multi-component	Concentration Prediction	Training-free	Noise-Robust
TagScan [63]	RFID	×	×	×	×
LiquID [10]	UWB	×	×	✓	✓
WiMi [11]	WiFi	×	×	×	✓
Vi-Liquid [21]	Vibration	✓	✓	✓	✓
FG-LiquID [35]	mmWave	×	×	×	✓
LiqRay [47]	RF	×	×	×	×
PackquID [48]	RF	×	×	✓	×
Akte-Liquid [55]	Acoustic	×	×	×	×
MetaBioLiq [7]	mmWave	×	×	×	✓
LiqDetector [64]	mmWave	×	×	✓	✓
Nutrilyzer [43]	Photoacoustic	✓	✓	×	✓
Al-light [37]	NIR & Visible Light	✓	✓	×	×
Jiang et al. [26]	NIR	×	✓	×	✓
CapCam [72]	Visible Light	×	✓	✓	✓
Li et al. [33]	Polarimetry	×	✓	×	✓
Lili [22]	Visible Light	×	×	✓	✓
Chan et al. [6]	NIR	×	×	×	×
BabyNutri [20]	Visible Light	✓	×	×	✓
GlucoSense [49]	Visible+NIR	×	✓	×	✓
MobiLyzer [38]	NIR & Visible Light	✓	✓	×	×
T-Oil [53]	Terahertz	✓	✓	×	×
MoleSen [52]	Terahertz	×	✓	×	✓
Polarix	**Polarimetry**	✓	✓	✓	✓

2.1.2 Optical Liquid Sensing. Optical signals sidestep multipath and offer higher chemical specificity. Photoacoustic sensing [43], NIR spectroscopy [6, 26, 34], and visible-light methods including absorption [20, 22, 37, 72] and polarimetry [33] have all been explored for liquid characterization. Recent work has pushed optical sensing onto mobile platforms: MobiSpectral [50] reconstructs hyperspectral bands from an unmodified smartphone's RGB and NIR cameras to detect food fraud, MobiLyzer [38] fuses RGB and NIR signals for fine-grained liquid analysis in everyday environments, and GlucoSense [49] exploits the optical activity of glucose to enable non-invasive monitoring on commodity phones. Beyond visible and NIR bands, terahertz-based systems have emerged: T-Oil [53] detects edible oil adulteration contactlessly, and MoleSen [52] probes molecular spectral signatures for taste sensing. Yet all these systems share a critical limitation in multi-component optically active liquids: they rely on either non-selective bulk optical properties or training-intensive chemometric models, neither of which can algebraically decouple individual substance concentrations from a single aggregate measurement.

■ **Novelty.** To the best of our knowledge, Polarix is the first sensing platform to overcome the linear superposition barrier of traditional polarimetry for multi-component liquid analysis. Unlike wireless or spectroscopic approaches that rely on environment-specific models, Polarix exploits differential temperature-dependent optical rotation across substances to **algebraically decouple individual concentrations**, a capability no prior polarimetric or mobile sensing system has achieved. A physical pilot marker on the rotating analyzer further enables **drift-immune, turbidity-robust optical rotation measurement**, yielding a **training-free $100 platform** that is simultaneously multi-component, concentration-predictive, and noise-robust, a combination no existing system achieves (Tab. 1).



(a) Glucose. (b) Xylose. (c) Fructose. (d) Lactic acid. (e) Lysine.

(f) Threonine. (g) Alanine. (h) Proline. (i) Arginine. (j) Isoleucine.

Figure 2: Temperature-dependent specific optical rotation of substances across 35°C–50°C.

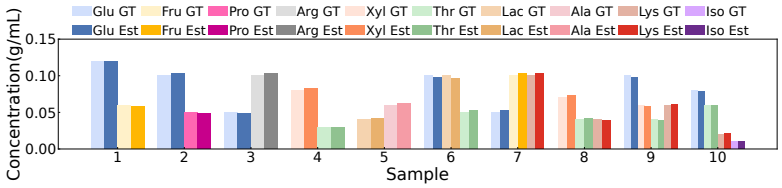


Figure 3: Estimated (Est) versus ground-truth (GT) concentrations across mixture samples, confirming accurate per-substance recovery.

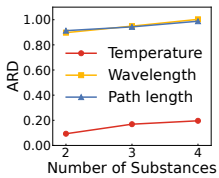


Figure 4: Comparison of modulation schemes.

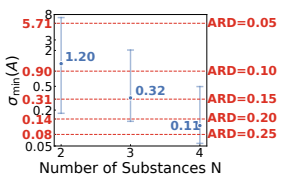


Figure 5: Separability across substance combinations.

2.2 Multi-Component Optically Active Liquid Monitoring

Precisely tracking multi-component optically active liquids is essential in biomanufacturing [39, 65, 71, 73] and food authentication [4, 61, 67]. The gold standards are HPLC [12, 16], enzymatic assays [30], and mass spectrometry [40, 59]: accurate but manual and offline, introducing hours of latency that preclude real-time process control. Inline spectroscopic alternatives such as NIR [34] and fluorescence [18] reduce this latency yet impose prohibitive hardware costs ($30,000–$50,000) and rely on environment-specific chemometric models, such as PLS or neural networks, that degrade across deployment scenarios. Conventional single-wavelength polarimeters face a more fundamental bottleneck: they measure only the linear superposition of all optically active components [25], producing a single aggregate rotation that is algebraically insufficient to distinguish individual substances. Polarix resolves this bottleneck at $100 with no training data. By exploiting differential temperature-dependent optical rotation, it transforms an otherwise underdetermined system into a solvable one, enabling robust inline concentration tracking of multiple substances simultaneously.

3 Preliminary

This section addresses three key questions that motivate Polarix: (1) how optical activity is measured and why one measurement cannot resolve mixtures; (2) why temperature, unlike path length or wavelength, makes an N-component mixture identifiable and how to assess separability for a new substance set; and (3) why classical rotation methods fail in real liquids, motivating our robust polarimetric system.

3.1 Measuring Optical Activity via Polarized Light

When polarized light traverses an optically active substance, its polarization plane rotates by an angle proportional to the substance's concentration and path length. The two dominant measurement methods are the intensity-based approach [36], which infers rotation from the ratio of transmitted to maximum intensity, and the half-shade method [24], which splits the beam into two paths and rotates the analyzer until both appear equally bright, reducing ambient-light sensitivity by differential referencing. Polarimetric sensing has been explored for glucose monitoring [33] and biomedical

diagnostics [58]. **The core challenge is that every optically active substance contributes to rotation simultaneously; recovering individual concentrations from a single aggregate measurement is algebraically underdetermined.**

3.2 Decoupling Multiple Substances via Temperature Modulation

We analyze under what conditions multiple-measurement polarimetry can resolve individual concentrations, and show that temperature modulation, unlike path-length or wavelength variation, yields a uniquely solvable system. The observed optical rotation α obeys Biot's law [8]:

$$\alpha = [\alpha]_\lambda^T \cdot l \cdot c \tag{1}$$

where $[\alpha]_\lambda^T$ is the specific rotation at wavelength λ and temperature T, l is the path length, and c is the concentration. For an N-component mixture, the additive principle [60] gives:

$$\alpha_{\text{total}} = \sum_{i=1}^{N} [\alpha_i]_\lambda^T \cdot l \cdot c_i \tag{2}$$

Recovering N unknown concentrations requires $M \geq N$ linearly independent equations. Taking M measurements under varying conditions (path length l, wavelength λ, or temperature T) yields the system:

$$l \cdot \begin{pmatrix} [\alpha_1]_{\lambda_1}^{T_1} & [\alpha_2]_{\lambda_1}^{T_1} & \cdots & [\alpha_N]_{\lambda_1}^{T_1} \\ [\alpha_1]_{\lambda_2}^{T_2} & [\alpha_2]_{\lambda_2}^{T_2} & \cdots & [\alpha_N]_{\lambda_2}^{T_2} \\ \vdots & \vdots & \ddots & \vdots \\ [\alpha_1]_{\lambda_M}^{T_M} & [\alpha_2]_{\lambda_M}^{T_M} & \cdots & [\alpha_N]_{\lambda_M}^{T_M} \end{pmatrix} \begin{pmatrix} c_1 \\ c_2 \\ \vdots \\ c_N \end{pmatrix} = \begin{pmatrix} \alpha_{\lambda_1} \\ \alpha_{\lambda_2} \\ \vdots \\ \alpha_{\lambda_M} \end{pmatrix} \tag{3}$$

We now examine each candidate modulation axis.

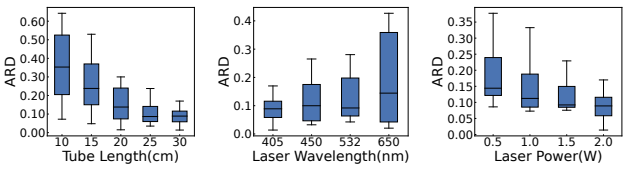
(1) Multiple measurements at different path lengths. Varying l scales every row of the coefficient matrix by the same factor, making all M equations linearly dependent. The system has infinitely many solutions; individual concentrations cannot be recovered.

(2) Multiple measurements at different wavelengths. The single-resonance Drude model gives the specific rotation at a fixed temperature T_0 as [42]:

$$[\alpha_i]_\lambda^{T_0} = \frac{k_i}{\lambda^2 - \lambda_0^2} \tag{4}$$

where k_i is a substance-specific constant and λ_0 is the absorption resonance wavelength.

Substituting Eq. 4 into Eq. 3 shows that, for a measurement taken at wavelength λ_m, all coefficients share the same scalar factor $1/(\lambda_m^2 - \lambda_0^2)$. As a result, each row of the coefficient matrix is simply a scaled version of the same vector $(k_1, k_2, \ldots, k_N)$. The rows are therefore linearly dependent, meaning the coefficient matrix has zero determinant and cannot be inverted. Consequently, even with measurements at multiple wavelengths, the resulting system of equations remains underdetermined.



(a) Impact of tube length (b) Impact of light wavelength (c) Impact of laser power.

Figure 6: Impact of tube length, light wavelength, and laser power.

(3) Multiple measurements at different temperatures. Unlike wavelength, the temperature dependence of specific optical rotation is substance-specific and lacks a universal dispersion law that would impose a shared functional form across substances [13, 66]. Golub et al. [13] showed that even the sign of the temperature gradient can differ across substances. Because no common factor can be extracted from the rows, the $M \times N$ coefficient matrix in the temperature-modulated system,

$$l \cdot \begin{pmatrix} [\alpha_1]^{T_1} & [\alpha_2]^{T_1} & \cdots & [\alpha_N]^{T_1} \\ [\alpha_1]^{T_2} & [\alpha_2]^{T_2} & \cdots & [\alpha_N]^{T_2} \\ \vdots & \vdots & \ddots & \vdots \\ [\alpha_1]^{T_M} & [\alpha_2]^{T_M} & \cdots & [\alpha_N]^{T_M} \end{pmatrix} \begin{pmatrix} c_1 \\ c_2 \\ \vdots \\ c_N \end{pmatrix} = \begin{pmatrix} \alpha^{T_1} \\ \alpha^{T_2} \\ \vdots \\ \alpha^{T_M} \end{pmatrix} \tag{5}$$

has full column rank in general, yielding a unique concentration solution.

■ **Proof of Principle.** To validate this, we measured the temperature-dependent specific optical rotation of 10 representative optically active substances using a commercial temperature-controlled polarimeter across a 35°C–50°C window. As shown in Fig. 2, each substance exhibits a distinct trend with temperature. We empirically model $[\alpha]^T$ using a third-order polynomial (solid curves in Fig. 2), a common low-order empirical form that adequately fits all ten calibration curves over 35–50°C under a single, substance-agnostic model. This uniform model ensures that the calibrated $[\alpha_i]^{T_m}$ entries of the design matrix A and the $\sigma_{\min}(A)$ separability metrics are directly comparable across substance sets.

To illustrate the identifiability condition, consider the simplest case: a two-substance mixture whose temperature responses are locally approximated as $[\alpha_1]^T \approx \omega_1 T + b_1$ and $[\alpha_2]^T \approx \omega_2 T + b_2$. Substituting into Eq. 5 and evaluating the 2×2 coefficient determinant at two temperatures $T_1 \neq T_2$ yields $(T_1 - T_2)(\omega_1 b_2 - b_1 \omega_2)$. A unique solution therefore exists if and only if $\frac{\omega_1}{\omega_2} \neq \frac{b_1}{b_2}$. This non-proportionality condition is readily satisfied when two substances differ in either slope or intercept. For $N > 2$ components, the general identifiability requirement is that the N column vectors of A_T

in Eq. 5, each representing a substance's specific-rotation values sampled across M temperatures, are linearly independent. Because the molecular origins of temperature sensitivity (conformational flexibility, solvation effects, and vibrational coupling) differ across chemically distinct species, we empirically observe that the $[\alpha](T)$ curves of different substances exhibit small but nonzero, substance-specific curvature (Fig. 2), and the resulting temperature–rotation profiles are sufficiently rich to maintain full column rank.

We first determine three key optical parameters, including the light wavelength, laser power, and optical path length, to establish the measurement conditions. As shown in Fig. 6, we selected a short violet wavelength of 405 nm because shorter wavelengths produce larger optical rotations and thus improve the signal-to-noise ratio, while green light at 532 nm is used for strongly absorbing or turbid liquids where optical penetration is more important; although infrared light provides greater penetration, the corresponding equipment is substantially more expensive, costing approximately $25,000. We also selected a 2 W laser to enhance optical contrast without excessive energy and a 30 cm optical path length to amplify the rotation signal while maintaining acceptable beam attenuation and system size. We prepared 10 samples with known concentrations, measured the aggregate optical rotation of each sample at multiple temperatures within the 35°C–50°C range, and estimated all component concentrations using a least-squares estimator with the calibrated specific-rotation curves as the design matrix. Fig. 3 shows that the estimated concentrations closely match the ground truth across all substances and samples. Furthermore, Fig. 4 shows that, among the three modulation axes we analyze, temperature modulation is the one that makes the mixture identifiable: temperature sweeps yield median ARDs of 0.09–0.20 for $N = 2$–4, whereas wavelength and path-length sweeps produce rank-deficient systems, with ARDs remaining at 0.8–1.0.

■ **Separability Guidance.** For deployment, consider a set of N substances measured at M temperatures. We define the design matrix $A \in \mathbb{R}^{M\times N}$ by $A_{m,i} = [\alpha_i]^{T_m} \cdot l$, where $[\alpha_i]^{T_m}$ is the calibrated specific rotation of substance i at temperature T_m, and l is the optical path length. We quantify the separability of the set by the smallest singular value $\sigma_{\min}(A)$: a small value indicates that two or more response columns are nearly linearly dependent and therefore difficult to distinguish, whereas a larger value indicates better-conditioned concentration recovery. The computed $\sigma_{\min}(A)$ can then be compared with the horizontal ARD reference lines in Fig. 5; a value above a given line indicates that the set is expected to achieve the corresponding ARD or lower. The figure reports median $\sigma_{\min}(A)$ values of 1.20, 0.32, and 0.11 over all $\binom{10}{N}$ substance combinations for $N = 2, 3, 4$, respectively. These medians fall between the ARD reference lines and predict typical ARDs of approximately 0.09, 0.15, and 0.22.

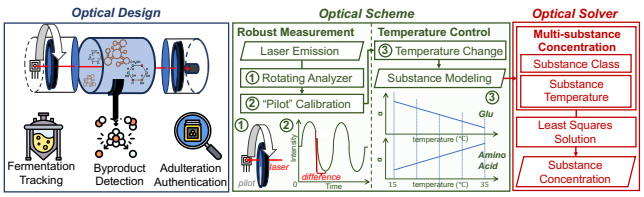


Figure 7: Overview of Polarix: a rotating analyzer with physical pilot marker measures optical rotation robustly, and temperature modulation enables training-free multi-substance concentration estimation.

3.3 Instability in Optical Rotation Measurement

Deploying polarimetry inline requires accurately measuring aggregate optical rotation across varying temperatures. However, in real-world deployments, target liquids are often turbid, colored, or dynamically flowing. Such conditions severely corrupt both traditional measurement methods, as illustrated in Fig. 8. We state that current methods for measuring optical rotation cannot work under these conditions.

Intensity-based method. When the incident polarized light and analyzer are initially aligned, the maximum intensity I_0 is obtained. With an optically active sample (rotation α_{test}), the received intensity follows Malus's law [5]:

$$I_{\text{rec}} = I_0 \cos^2(\alpha_{\text{test}}) + \sigma_{\text{rec}} \tag{6}$$

where σ_{rec} captures intensity perturbations from turbidity and flow. Since I_0 is itself unstable in such environments, the inferred α_{test} is corrupted by σ_{rec} and the uncertainty in I_0.

Half-shade method. The analyzer is rotated until the glass path and quartz path appear equally bright:

$$I_{\text{glass}} = I_0 \cos^2\left(\alpha_{\text{test}} - \frac{\alpha_{\text{quartz}}}{2}\right) + \sigma_{\text{glass}} \tag{7}$$

$$I_{\text{quartz}} = I_0 \cos^2\left(\alpha_{\text{test}} + \frac{\alpha_{\text{quartz}}}{2}\right) + \sigma_{\text{quartz}} \tag{8}$$

Although differential referencing between the two paths partially cancels common-mode noise, spatial inhomogeneities in the distorted beam cause $\sigma_{\text{glass}} \neq \sigma_{\text{quartz}}$, making the balance condition unreliable and producing systematic errors in the estimated α_{test}. A measurement approach that is robust to such intensity noise is therefore required.

4 Polarix System

Design at a glance. Fig. 7 illustrates a single measurement by Polarix, with each stage corresponding to a subsection below. **(1) Read** (Sec. 4.1): A sample-filled tube is placed between a fixed polarizer and a continuously rotating analyzer, while a photodiode records the transmitted intensity. Polarix infers optical rotation from the phase of minimum

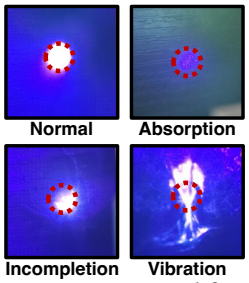


Figure 8: Environmental factors distort the transmitted light spot: coloration increases absorption, suspended particles corrupt beam integrity, and fluid motion causes vibration.

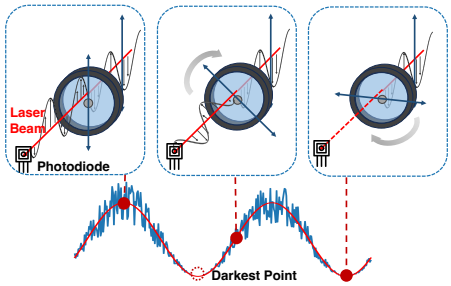


Figure 9: Polarix tracks the minimum-intensity phase of the rotating analyzer. Despite intensity fluctuations (blue) versus stable conditions (red), the inferred optical rotation remains consistent.

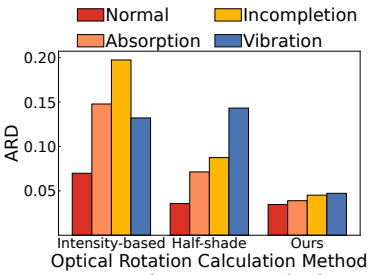


Figure 10: Under varying light-spot conditions, Polarix maintains stable optical rotation readings for lysine, while intensity-based and half-shade methods degrade significantly.

intensity, rather than its amplitude, making the measurement robust to color, suspended solids, and flow. **(2) Sweep** (Sec. 4.2): The tube is heated once and measured continuously during slow cooling, yielding M rotation values at M temperatures in a single sweep. A light-blocking pilot strip on the analyzer re-references each rotation cycle, preventing period jitter from a low-cost stepper motor from accumulating. **(3) Solve** (Sec. 4.3): The M readings are stacked into $\boldsymbol{\alpha}$ and inverted using the design matrix A defined in Eq. 5, recovering all N concentrations simultaneously without training data or per-site recalibration.

4.1 Robust Optical Rotation Measurement

To measure the concentrations of multiple optically active substances based on the temperature-dependent nature of their optical rotations, we should accurately determine the optical rotation under varying temperatures. However, the intensity-based and half-shade methods introduced in Sec. 3.1 rely heavily on the quality of the light spot. In the real world, changes in liquid color, suspended particles, and fluid flow can significantly affect spot quality (Fig. 8), leading to measurement instability. Consequently, a robust optical rotation measurement technique is urgently needed.

Revisiting the property of optical rotation. Let the polarizer axis form angle θ_0 with the horizontal. After traversing an optically active sample with rotation α, the light's polarization direction becomes $\theta_0 + \alpha$. When the analyzer is positioned at angle θ_1, Malus's law [5] gives the transmitted intensity as:

$$I = I_0 \cos^2\big((\theta_0 + \alpha) - \theta_1\big) \tag{9}$$

We are interested in the case that is least affected by light intensity, so we focus on **the darkest point**. The intensity reaches zero when $(\theta_0 + \alpha) - \theta_1 = 90°$, yielding:

$$\alpha = 90° + \theta_1 - \theta_0 \tag{10}$$

Critically, this darkest-point condition depends solely on polarization angles and is **independent of the incident intensity** I_0. Even when the beam is attenuated or distorted by turbid or colored media, the minimum-intensity position is largely unaffected, providing a measurement that is robust to intensity noise.

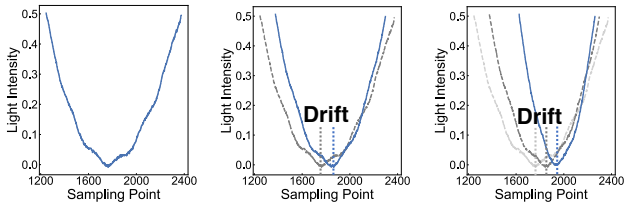
Darkest-point detection. As shown in Fig. 9, we propose an automated detection approach using a photodiode and a **rotatable analyzer**. We mount the analyzer on a stepper motor for continuous rotation and use a photodiode to record transmitted intensity. By symmetry, at least one intensity minimum occurs per half-revolution. Let fs denote the photodiode sampling rate and t the half-revolution duration. We first record the air-reference darkest position pos_{air}. During liquid measurement, the analyzer rotates from pos_{air} and the minimum occurs at sample index $sp_{\min}$. The optical rotation is then:

$$\alpha = \begin{cases} \dfrac{sp_{\min}}{t \cdot fs} \cdot 180°, & sp_{\min} \le \dfrac{t \cdot fs}{2}, \\ 90° - \dfrac{sp_{\min}}{t \cdot fs} \cdot 180°, & sp_{\min} > \dfrac{t \cdot fs}{2}. \end{cases} \tag{11}$$

Because intensity near the true minimum is very flat, pinpointing $sp_{\min}$ in a single cycle is noisy. We therefore average $sp_{\min}$ across multiple consecutive cycles to suppress this uncertainty. Fig. 10 confirms that our method maintains stable optical rotation readings under fluctuating intensity, whereas intensity-based and half-shade methods degrade substantially.

4.2 Enabling Stable Measurement During Temperature Changes

Decoupling multiple substances requires consistent optical rotation measurements across a full temperature sweep. During a prolonged cooling cycle, however, measurement error gradually accumulates. We investigated by continuously



(a) Early stage. (b) Mid-term. (c) Later stage.

Figure 11: Cumulative motor drift progressively shifts the detected darkest point across cycles, degrading optical rotation accuracy over a long temperature sweep.

measuring water, which has zero optical activity and should yield a constant rotation reading. As shown in Fig. 11, the detected darkest position drifts progressively later within each cycle.

The root cause is that the stepper motor's half-revolution duration is not exactly t but $t + t_{\sigma,k}$, where $t_{\sigma,k}$ is a small random deviation in cycle k. Using a fixed period t to divide the timeline, the darkest-point position accumulates as:

$$sp_{\text{drift}} = \sum_{i=1}^{k} t_{\sigma,i} \cdot fs \tag{12}$$

This cumulative shift grows unboundedly over time and directly corrupts the rotation reading.

Pilot strip solution. To address this, we propose the addition of a **light-blocking strip** on the analyzer. Once per revolution, the strip occludes the beam, producing a sharp intensity drop that is easily distinguished from the gradual darkening near the optical minimum. We call this event the **pilot**. As shown in Fig. 12, the strip is placed at position OA. During air calibration, we orient OA such that positions OB and OC (both 90° from OA) coincide with the darkest points. This geometry places OA at the theoretical intensity peak, maximizing the contrast of the pilot drop for reliable detection, and simultaneously preserves the full ±90° optical rotation measurement range.

With the pilot, each cycle is re-referenced to sp_{pilot} rather than a fixed period, reducing the per-cycle drift to:

$$\hat{sp}_{\text{drift}} = \frac{t_{\sigma,k}}{t} \cdot fs \tag{13}$$

Because $t_{\sigma,k} \ll t$ and is nearly zero-mean random noise, averaging over multiple cycles suppresses this residual drift to a negligible level.

The updated optical rotation formula using the pilot reference is:

$$\alpha = \begin{cases} \dfrac{sp_{\min} - sp_{\text{pilot}}}{t \cdot fs} \cdot 180°, & sp_{\min} \le \dfrac{t \cdot fs}{2} + sp_{\text{pilot}}, \\ 90° - \dfrac{sp_{\min} - sp_{\text{pilot}}}{t \cdot fs} \cdot 180°, & sp_{\min} > \dfrac{t \cdot fs}{2} + sp_{\text{pilot}}. \end{cases} \tag{14}$$

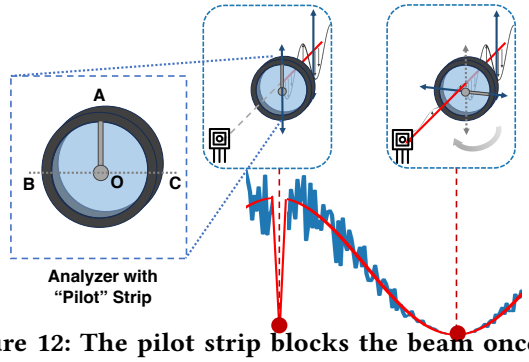
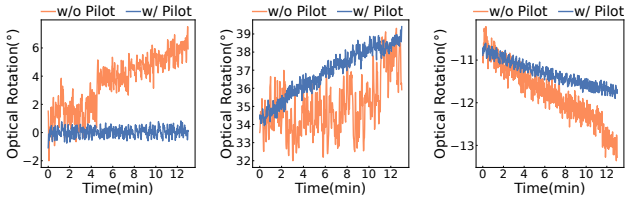


Figure 12: The pilot strip blocks the beam once per cycle, marking each cycle's origin. Positioning OA at the theoretical brightness peak ensures a sharp, unambiguous pilot signal and preserves the full ±90° measurement range.



(a) Water. (b) Glucose. (c) Threonine.

Figure 13: With the pilot, optical rotation remains stable over a full temperature sweep: water holds near 0°, and both glucose and threonine exhibit the expected monotonic temperature trends.

Fig. 13 validates the approach: with the pilot enabled, water's optical rotation stabilizes near 0° throughout the entire sweep, confirming that drift is eliminated, while glucose and threonine display clean, monotonic temperature-dependent trends suitable for concentration estimation. A natural alternative is to use an encoder. However, it would require an additional clock synchronized with the photodiode to align the measured light intensity with the analyzer's rotation angle, whereas the pilot strip achieves this directly.

4.3 Multi-Substance Concentration Estimation

Given stable temperature-variant optical rotation measurements, we now describe the training-free solver that recovers individual substance concentrations. For each of the N target substances, we measure the temperature-dependent specific rotation $[\alpha_i]^T$ using standard solutions of known concentration, obtaining via $[\alpha_i]^T = \alpha^T/(l \cdot c)$. Multiple standard concentrations are averaged to reduce calibration error. This calibration is performed once and applies to all subsequent measurements, regardless of sample origin or matrix.

Concentration solver. Let $\hat{c}_i$ denote the predicted concentration of substance i. Using the calibrated specific-rotation

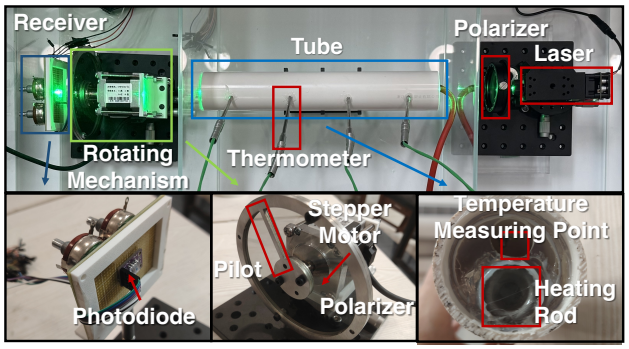


Figure 14: Prototype of Polarix. The sensing tube (center) houses the heating element and thermocouple; the rotating analyzer with pilot strip (right) is driven by the stepper motor; the photodiode receiver (left) feeds into the embedded controller.

curves, the predicted aggregate optical rotation at temperature T_m is:

$$\hat{\boldsymbol{\alpha}} = \underbrace{\begin{pmatrix} [\alpha_1]^{T_1} \cdot l & \cdots & [\alpha_N]^{T_1} \cdot l \\ [\alpha_1]^{T_2} \cdot l & \cdots & [\alpha_N]^{T_2} \cdot l \\ \vdots & \ddots & \vdots \\ [\alpha_1]^{T_M} \cdot l & \cdots & [\alpha_N]^{T_M} \cdot l \end{pmatrix}}_{A \in \mathbb{R}^{M \times N}} \begin{pmatrix} \hat{c}_1 \\ \vdots \\ \hat{c}_N \end{pmatrix} \tag{15}$$

where the design matrix A is constructed from offline calibration data. The observed rotation vector is $\boldsymbol{\alpha} = (\alpha^{T_1}, \alpha^{T_2}, \ldots, \alpha^{T_M})^\top$. With $M \geq N$ measurement temperatures, the overdetermined system is solved via constrained least squares:

$$\min_{\hat{\mathbf{c}} \geq \mathbf{0}} \frac{1}{M} \left\| \boldsymbol{\alpha} - A\hat{\mathbf{c}} \right\|_2^2 \tag{16}$$

The non-negativity constraint $\hat{\mathbf{c}} \geq \mathbf{0}$ reflects the physical requirement that concentrations cannot be negative. We solve this using the L-BFGS-B optimizer, a bound-constrained quasi-Newton method that scales efficiently with N. No training data, domain-specific models, or environment-specific calibration are required beyond the one-time specific-rotation characterization.

5 Evaluation

5.1 Experimental Setup

We introduce the prototype, ground-truth acquisition, test liquids, and metrics. Every experiment was repeated 5 times and the median is reported.

5.1.1 Prototype. As shown in Fig. 14, Polarix consists of several key components. A 2 W, 405 nm coherent OXLaser module ($12.3) generates a laser beam that is linearly polarized by a GKM-0104 polarizer ($1.56). The beam passes through a 30cm tube (≈ $0.1) containing a 3 kW heating rod ($3.83) and four K-sheathed thermocouple thermometers ($28.71) mounted at the top to measure the internal temperature; the tube is wrapped in rubber insulation to retard heat loss during the cooling ramp. The rotating mechanism is driven by a 57BYG250 stepper motor ($17.57), which rotates the analyzer (≈ $1) with a light-blocking pilot strip affixed to a 3.0 mm Cr-304 stainless-steel support fabricated by wire-electrode cutting. An OPT101 photodiode [56] ($7.71) detects the transmitted light, and an Arduino UNO [2] ($12.97) collects photodiode samples. Total hardware cost is under **$100**.

5.1.2 Environment & Liquids. We evaluate Polarix across two distinct target categories. For system micro-benchmarks, end-to-end performance, and environmental robustness (Sec. 5.2–5.4), we use simulated solutions of optically active substances with known ground-truth concentrations (e.g., glucose, fructose, and specific amino acids). To demonstrate practical universality (Sec. 5.5.1–5.5.3), we deploy Polarix in three diverse real-world applications: dynamic multi-substance tracking in operational bioreactors, trace-byproduct detection in complex fermentation broth, and food-safety authentication of honey under industrial adulteration. Ground truth comes from liquid chromatography.

5.1.3 Metrics. We use two metrics to evaluate Polarix.
Absolute Relative Difference (ARD). ARD quantifies estimation accuracy across all substances and applications:

$$\text{ARD} = \frac{|c_{\text{ref}} - c_{\text{est}}|}{c_{\text{ref}}} \tag{17}$$

where c_{ref} is the ground-truth concentration and c_{est} is the estimated value. By normalizing against c_{ref}, ARD is scale-independent and directly comparable across substance types and concentration ranges. When reporting an overall ARD across applications, we compute the macro-average: the ARD of each substance in each experiment is first averaged within that experiment, and the resulting per-experiment means are then averaged across all experiments with equal weight. An ARD within 20% is considered acceptable [15].
Energy Consumption. We determine energy consumption from the power of each module and its operating duration:

$$E = (P_{\text{laser}} + P_{\text{motor}}) \cdot t + E_{\text{heater}} \tag{18}$$

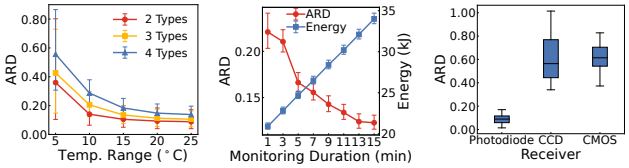
where P_{laser} and P_{motor} are the laser and motor power, and E_{heater} is the energy consumed during one heating cycle. The laser and motor operate only during the cooling phase when optical rotation is measured; the heater consumes energy only during the short heating ramp.

5.2 Micro-Benchmark

5.2.1 Impact of Temperature Range. Temperature modulation is the core knob in Polarix: a wider sweep improves multi-substance identifiability but increases perturbation of the sample environment. As shown in Fig. 15(a), a 5°C sweep

Table 2: Consolidated comparison of Polarix, its ablation settings, evaluated sensing baselines, and commercial/reference instruments in accuracy, throughput, automation, and deployment fit.

System	Setting	$ARD_{N=1}\downarrow$	$ARD_{N=2}\downarrow$	$ARD_{N=3}\downarrow$	$ARD_{N=4}\downarrow$	Throughput (samples/h)↑	Automation	Deployment fit
Polarix	Full system	**0.057**	**0.118**	**0.148**	**0.220**	4	✓	Per-vessel monitoring
	W/o T-Var	0.034	1.488	1.863	2.599			
	W/o Rotation	0.447	0.837	1.048	1.465			
	W/o Pilot	0.346	0.558	0.699	0.976			
Traditional optical-rotation methods								
Intensity polarimetry [70]		0.763	0.932	1.214	1.620	5	✗	Process polarimetry
Half-shade polarimeter [24]		0.418	0.493	0.593	0.734	5	✗	Manual polarimetry
Mobile sensing methods								
Vi-Liquid [21]		0.409	0.593	0.761	1.002	3	✗	Consumer screening
Al-light [37]		0.278	0.436	0.585	0.873	5	✗	In-glass sensing
Nutrilyzer [43]		0.142	0.236	0.361	0.524	3	✗	Food screening
High-precision, high-cost instruments								
NIR spectroscopy [51]		0.015	0.033	0.042	0.043	2	✓	At-line monitoring
Inline biosensor [23]		0.011	Single-substance only			1	✓	On-line glucose
HPLC / MS [12]		Reference-grade				0.5	✗	Reference assay



(a) Impact of temperature range. (b) Impact of monitoring duration. (c) Impact of light sensor.

Figure 15: Impact of temperature range, monitoring duration, and light sensor.

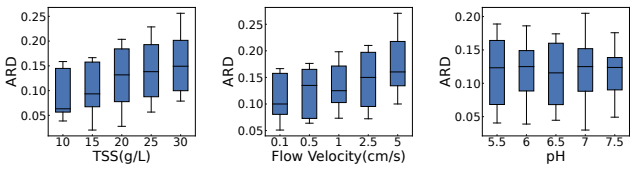
yields ARD of 0.448, while 15°C reduces it to 0.141; extending to 25°C reaches 0.111 but imposes a perturbation that may deviate heat-sensitive samples from their optimal operating temperature (even though many microorganisms tolerate ~20°C changes). We therefore adopt 15°C as the operating point, providing sufficient identifiability while minimizing sample disturbance. The method is not limited to a 15°C span within 35–50°C and can be adapted to any temperature window suitable for the application.

5.2.2 Impact of Monitoring Duration. Measurements are taken during cooling, since rapid heating can destabilize the liquid. A 15°C ramp typically takes ≈15 min, but continuously rotating the analyzer throughout wastes energy and accelerates mechanical wear. Fig. 15(b) shows that operating the analyzer intermittently for 10 min within each 15 min measurement achieves an ARD of 0.135 while saving ≈5 kJ; we therefore adopt this duty cycle by default. Because Polarix targets long-horizon monitoring, concentrations remain effectively constant over the full 15 min measurement. At a lysine production rate of 2.57 g/L/h, the concentration changes by only 0.00064 g/mL during this interval, while static samples such as honey do not change, making intra-sweep drift negligible.

5.2.3 Impact of Light Sensor. Fig. 15(c) shows that a photodiode receiver achieves the lowest ARD (0.102), owing to its high sampling frequency which faithfully captures the minimum-intensity phase. Camera-based receivers (CCD, CMOS) introduce higher latency and lower effective sampling rates because they must transfer and process significantly more data, making them unsuitable for rapid phase detection. We therefore use a photodiode in all subsequent experiments.

5.3 Overall Performance

Design Contribution. We evaluate how each of Polarix's three core components contributes to accuracy as mixture complexity grows from 1 to 4 coexisting substances (Tab. 2). Without temperature modulation (W/o T-Var), ARD starts at 0.034 for a single substance and escalates sharply to 2.599 at four substances, confirming that temperature-induced rotation diversity is the mathematical prerequisite for multi-substance identifiability, as the system becomes increasingly unsolvable without it. Without the rotating analyzer (W/o Rotation), ARD similarly climbs from 0.447 to 1.465, as static intensity measurement conflates polarization angle with amplitude fluctuations from turbidity and flow, a bias that compounds with each additional substance. Without pilot-based drift correction (W/o Pilot), ARD grows more moderately from 0.346 to 0.976, yet the degradation remains consistent across all mixture sizes, since cumulative motor drift introduces a persistent rotation offset that contaminates every substance's estimate. Polarix with all three components



(a) Impact of Turbidity. (b) Impact of Flow Rate. (c) Impact of pH.

Figure 16: ARD under varying real-world liquid conditions: (a) turbidity (TSS), (b) flow rate, and (c) pH.

achieves ARD of 0.057 at one substance, rising only to 0.220 at four substances, remaining nearly flat as mixture complexity increases, a scalability that no partial design attains.

Comparison with Baselines. We compare Polarix with existing sensing methods and reference instruments in accuracy, throughput, automation, and deployment fit (Tab. 2). As mixture complexity increases from 1 to 4 substances, all evaluated sensing baselines show substantial accuracy degradation. The ARD of intensity polarimetry rises from 0.763 to 1.620, half-shade polarimetry from 0.418 to 0.734, Vi-Liquid from 0.409 to 1.002, Al-light from 0.278 to 0.873, and Nutrilyzer from 0.142 to 0.524. These methods measure aggregate optical, vibrational, absorption, or photoacoustic responses without explicitly decoupling individual substances, causing estimation errors to accumulate as more components coexist. In contrast, Polarix maintains substantially lower ARD, increasing only from 0.057 to 0.220, demonstrating robust multi-substance separability. NIR spectroscopy achieves higher accuracy but lower throughput and typically relies on matrix-specific chemometric calibration, while the inline biosensor is restricted to a single target substance. HPLC/MS provides reference-grade measurements but requires offline laboratory analysis and approximately two hours per sample. Polarix instead provides four autonomous multi-substance measurements per hour.

5.4 Environmental Robustness

We evaluate Polarix's robustness under three real-world liquid conditions that challenge optical sensing: turbidity, flow, and pH variation.

5.4.1 Impact of Turbidity. We introduce solid suspensions spanning a concentration range (10–30 g/L TSS), which spans typical industrial broth solid loads [44]. At 30 g/L with a 2 W laser, the received light power remains ≈10 mW, which is within the photodiode's measurable range. As shown in Fig. 16(a), ARD increases from 0.060 to 0.155 as TSS rises from 10 to 30 g/L, confirming that Polarix maintains acceptable accuracy across the full practical turbidity range.

5.4.2 Impact of Flow Rate. Liquid flow creates laminar-velocity gradients that expose polarized light to spatially inhomogeneous optical environments, causing polarimetric errors. Fig. 16(b) shows that increasing flow rate raises ARD by up to 0.065 and increases variance. Polarix achieves its best accuracy at lower flow rates; for inline deployments with fast-moving liquids, we recommend routing the sample through a low-flow bypass tube during measurement. The tested flow range reflects common bypass/sidestream rates used in industrial process monitoring [41, 54].

5.4.3 Impact of pH. The pH of target liquids can vary substantially depending on the application (e.g., around 7 in amino-acid fermentation, acidic in fruit juices or vinegar). We regulate pH with phosphoric acid and sodium hydroxide. As shown in Fig. 16(c), pH has no significant effect on measurement accuracy, with a maximum ARD of 0.125 across the full tested range, confirming that Polarix is pH-agnostic. This pH range encompasses the conditions targeted by Polarix [44].

5.5 Case Study

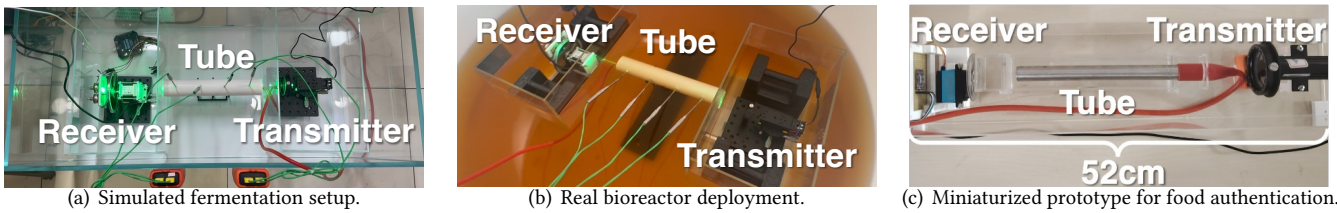
5.5.1 Amino Acid Fermentation Tracking. We deploy Polarix into operational bioreactors to autonomously track multi-substance conversions across 6–7 fermentation stages at 10-hour intervals, covering three commercial amino acid bioprocesses in both simulated and real environments (Fig. 18). We use a 532 nm laser to ensure sufficient beam penetration through turbid fermentation broth.

Threonine. Across glucose-based and xylose-based fermentations, Polarix achieves ARD of 0.116 for threonine, 0.086 for glucose, and 0.098 for xylose.

Lysine. In glucose-to-lysine bioprocesses, ARD is 0.133 for lysine and 0.074 for glucose, including real bioreactor deployments where microbial populations and broth opacity vary across stages.

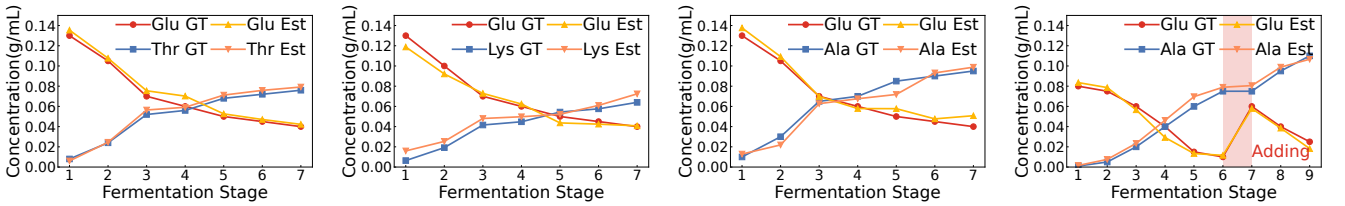
Alanine. Across glucose-based and lactic-acid-based conversions, including a dynamic mid-process glucose addition scenario, ARD is 0.162 for alanine, 0.089 for glucose, and 0.188 for lactic acid.

5.5.2 Trace Byproduct Detection. Industrial fermentation routinely generates low-concentration byproducts through branched metabolic routes, complicating monitoring and inflating purification costs. We evaluate Polarix's ability to resolve trace components within a complex dominant-species mixture. As shown in Fig. 19, Polarix simultaneously tracks primary targets and minority byproducts across up to four coexisting substances. For the three-component case, glucose ARD is 0.075 and threonine ARD is 0.089. For the four-component case with both lysine and isoleucine present as byproducts, their ARDs are 0.194 and 0.269, respectively, even at concentrations far below the dominant species. These results demonstrate Polarix's potential as an autonomous early-warning mechanism for process anomalies without any hardware reconfiguration or retraining.

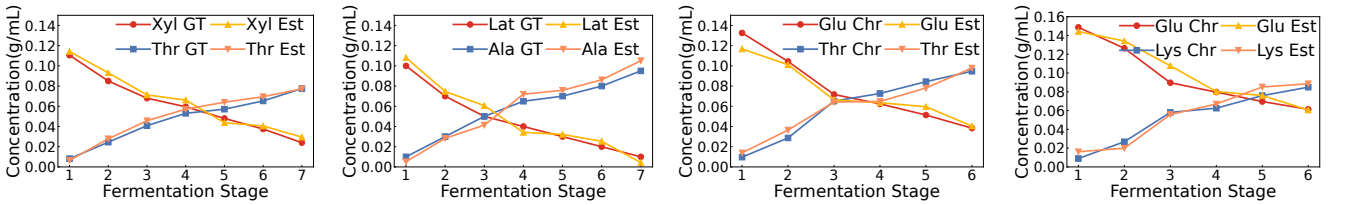


(a) Simulated fermentation setup. (b) Real bioreactor deployment. (c) Miniaturized prototype for food authentication.

Figure 17: Deployment configurations of Polarix: (a) simulated amino acid fermentation with controlled ground-truth concentrations, (b) real bioreactor deployment for in-situ fermentation tracking, and (c) miniaturized form factor for honey adulteration authentication.

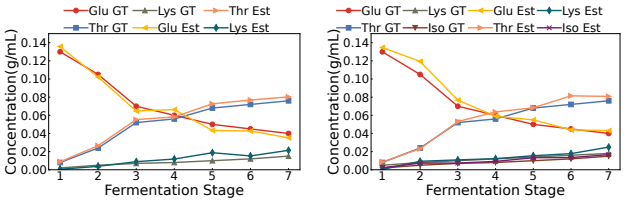


(a) Simulation: glucose - threonine. (b) Simulation: glucose - lysine. (c) Simulation: glucose - alanine. (d) Simulation: glucose - alanine, glucose addition.



(e) Simulation: xylose - threonine. (f) Simulation: lactate - alanine. (g) Real: glucose - threonine. (h) Real: glucose - lysine.

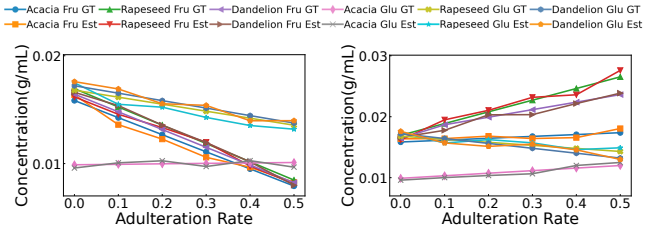
Figure 18: Fermentation tracking results across diverse substrate-to-amino-acid bioprocesses in both simulated (a–f) and real (g–h) bioreactor environments.



(a) In simulated glucose - threonine, lysine is a by-product. (b) In simulated glucose - threonine, lysine and isoleucine are by-products.

Figure 19: Simultaneous monitoring in the presence of trace amino acid byproducts: (a) lysine as a byproduct during glucose-to-threonine fermentation; (b) lysine and isoleucine as co-byproducts.

5.5.3 Honey Adulteration Authentication. We apply Polarix to food-safety authentication: detecting honey adulteration by recovering the native fructose-to-glucose ratio. A 10 mL honey sample dissolved in 300 mL water yields concentrations of 0.01–0.02 g/mL, within Polarix's polarimetric resolution. Three honey varieties (acacia, rapeseed, dandelion) were tested under rice-syrup and HFCS-55 adulteration at 10%–50% substitution rates. Rice-syrup adulteration causes fructose to decline monotonically from 0.018 g/mL to 0.007 g/mL across all varieties, as the fructose-free adulterant progressively dilutes native fructose; glucose remains relatively stable near 0.010 g/mL. In Fig. 20(b), HFCS-55 adulteration shifts



(a) Rice syrup adulteration. (b) HFCS-55 adulteration.

Figure 20: Honey adulteration authentication across three honey varieties (acacia, rapeseed, dandelion) under (a) rice-syrup and (b) HFCS-55 adulteration at 10%–50% substitution rates.

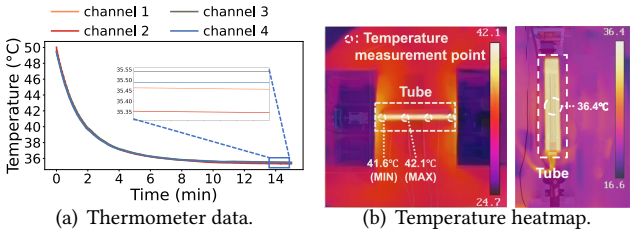
the sugar balance differently: fructose rises steeply from about 0.017 g/mL to 0.026 g/mL while glucose changes only mildly, reflecting the fructose-rich composition of HFCS-55.

As shown in Fig. 20, in both scenarios, Polarix's estimated concentrations track ground truth tightly across all three varieties and all adulteration levels, achieving overall ARD of 0.106.

6 Discussion

6.1 Limitations

First, deployments in sanitary-sensitive environments such as bioreactors require additional sterilization and sealing procedures for the sensing tube. Second, the 15°C thermal sweep



(a) Thermometer data. (b) Temperature heatmap.

Figure 21: Spatial and temporal temperature uniformity: (a) four thermocouple channels remain within a 0.5°C spread throughout the cooling ramp; (b) thermal imaging confirms a spatially uniform interior.

introduces a transient temperature deviation in the sampled volume; applications with strict isothermal requirements may need a dedicated bypass loop. Third, estimation accuracy degrades below 0.005 g/mL, constraining applicability to sufficiently concentrated solutions; extending the tube length can partially mitigate this. Fourth, ARD increases notably beyond four coexisting substances as the noise causes errors in calculations; nevertheless, our resolution already covers the dominant use cases in fermentation tracking and food authentication. Fifth, Polarix assumes a known substance set, while open-set identification of arbitrary unknown species remains future work. Sixth, our system cannot separate near-identical molecules such as isotopologues, which typically require costly specialized instruments to distinguish.

6.2 Impact of Temperature Perturbation

The 15°C sweep is applied only to the small liquid volume within the sensing tube, not to the bulk sample or process vessel. If the measured liquid is merely a withdrawn test sample, the temperature variation has no effect on the original system or production process. For in-situ industrial deployments, the sensing tube contains only a small sidestream volume isolated from the main reactor. To conservatively bound any production impact in the most demanding scenario, we assume microbial activity in the tube is fully suppressed during the 15-minute measurement. Even under this worst-case assumption, the loss is negligible: for lysine (production rate 2.57 g/L/h), the missed yield over 15 minutes is only 0.31 g, corresponding to less than 0.0005% of total output in a 100 m^3 industrial fermenter. This equates to less than 4.3 ms of additional fermentation time to compensate, confirming that the thermal perturbation has no meaningful impact on process yield in realistic deployments. Additionally, the 50°C upper bound remains well below the temperatures at which amino acids and sugars undergo thermal decomposition, preserving analyte integrity. For heat-labile species, the window can be shifted downward, since decoupling depends on relative rotation changes rather than absolute temperature.

6.3 Temperature Uniformity

Accurate multi-substance decoupling requires that all measurement points in a temperature sweep correspond to a well-defined, spatially uniform sample temperature. Because the heating rod spans the full tube length and the sampled volume is small, the liquid rapidly reaches a near-isothermal state. We validated this with thermal imaging and four-channel thermocouple logging. As shown in Fig. 21(a), all four temperature channels converge tightly throughout the cooling ramp, with a maximum spatial spread of 0.5°C (41.6–42.1°C) at any given time. The thermal heatmap in Fig. 21(b) confirms that the temperature gradient is confined to the tube wall, with the liquid interior remaining spatially uniform. A simulation analysis indicates that using the average temperature instead of the actual temperature distribution will only increase the ARD by 0.003, confirming that residual non-uniformity has no meaningful effect on multi-substance estimation accuracy.

6.4 Deployment Implications

Because Polarix costs about $100, which is two to three orders of magnitude less than inline NIR or biosensor instruments, it becomes practical to deploy them per vessel rather than share a handful of centralized analyzers. This capability is particularly valuable in parallel fermentation and other multi-vessel processes, where each vessel requires independent online monitoring but conventional analytical instruments remain too costly for dense deployment [29, 74]. This shifts multi-substance monitoring from sparse sampling and laboratory auditing to continuous, per-vessel visibility.

7 Conclusion

We present Polarix, a polarimetric platform that resolves multi-component concentrations by sweeping sample temperature, exploiting substance-specific thermal coefficients of optical rotation to convert an underdetermined single-observation problem into a solvable system. Across amino-acid fermentation tracking, trace byproduct detection, and honey adulteration screening, Polarix achieves an overall ARD of 0.121, demonstrating effective autonomous multi-substance monitoring in complex real-world liquids.

Acknowledgments

We would like to express our gratitude to all anonymous reviewers for their constructive comments. This work is supported in part by National Natural Science Foundation of China (No. 62602410), Natural Science Foundation of Shanghai (No. 24ZR1430600) and Shanghai Key Laboratory of Trusted Data Circulation and Governance, and Web3.

References

[1] Tsumoto Arakawa, K Tsumoto, Yet al Kita, B Chang, and D Ejima. 2007. Biotechnology applications of amino acids in protein purification and formulations. Amino acids 33, 4 (2007), 587–605.

[2] Arduino. [n. d.]. Arduino UNO R3. Arduino Documentation. https://docs.arduino.cc/hardware/uno-rev3/ Accessed January 19, 2026.

[3] NJ Berthels, RR Cordero Otero, FF Bauer, JM Thevelein, and IS Pretorius. 2004. Discrepancy in glucose and fructose utilisation during fermentation by Saccharomyces cerevisiae wine yeast strains. FEMS yeast research 4, 7 (2004), 683–689.

[4] Aroni Preya Biswas, Mahmuda Tasnim, Özge Süfer, Sagar Chandra Das, Shaswaty Sarker, Min Zhang, and Nahidul Islam. 2026. Honey adulteration detection: a comprehensive review of traditional and modern techniques. Journal of Food Measurement and Characterization 20, 4 (2026), 3929–3964.

[5] Caslav Brukner and Anton Zeilinger. 1999. Malus' law and quantum information. acta physica slovaca 49 (1999), 647–652.

[6] Justin Chan, Ananditha Raghunath, Kelly E Michaelsen, and Shyamnath Gollakota. 2022. Testing a drop of liquid using smartphone LiDAR. Proceedings of the ACM on Interactive, Mobile, Wearable and Ubiquitous Technologies 6, 1 (2022), 1–27.

[7] Baicheng Chen, John Nolan, and Xinyu Zhang. 2024. MetaBioLiq: A wearable passive metasurface aided mmWave sensing platform for BioFluids. In Proceedings of the 30th Annual International Conference on Mobile Computing and Networking. 1192–1206.

[8] Jonathan Clayden, Nick Greeves, and Stuart Warren. 2012. Organic chemistry. Oxford university press.

[9] Martina D'Este, Merlin Alvarado-Morales, and Irini Angelidaki. 2018. Amino acids production focusing on fermentation technologies–A review. Biotechnology advances 36, 1 (2018), 14–25.

[10] Ashutosh Dhekne, Mahanth Gowda, Yixuan Zhao, Haitham Hassanieh, and Romit Roy Choudhury. 2018. Liquid: A wireless liquid identifier. In Proceedings of the 16th annual international conference on mobile systems, applications, and services. 442–454.

[11] Chao Feng, Jie Xiong, Liqiong Chang, Ju Wang, Xiaojiang Chen, Dingyi Fang, and Zhanyong Tang. 2019. WiMi: Target material identification with commodity Wi-Fi devices. In 2019 IEEE 39th international conference on distributed computing systems (ICDCS). IEEE, 700–710.

[12] Mireille Ginésy, Josefine Enman, Daniela Rusanova-Naydenova, and Ulrika Rova. 2019. Simultaneous quantification of L-Arginine and monosaccharides during fermentation: an advanced chromatography approach. Molecules 24, 4 (2019), 802.

[13] Morton A Golub and Edward E Pickett. 1954. Effect of temperature and pH on the optical rotation of proteins. Journal of Polymer Science 13, 71 (1954), 427–440.

[14] Grand View Research. 2024. Lysine Market Size, Share And Trends Report, 2024–2030. Grand View Research. https://www.grandviewresearch.com/industry-analysis/lysine-market

[15] IH Guideline. 2022. Analytical procedure development Q14. International council for Harmonisation of technical requirements for pharmaceuticals for human use: Geneva, Switzerland (2022).

[16] Valoran P Hanko and Jeffrey S Rohrer. 2004. Determination of amino acids in cell culture and fermentation broth media using anion-exchange chromatography with integrated pulsed amperometric detection. Analytical biochemistry 324, 1 (2004), 29–38.

[17] Thomas Hermann. 2003. Industrial production of amino acids by coryneform bacteria. Journal of biotechnology 104, 1-3 (2003), 155–172.

[18] Jhonatan A Hernandez-Valdes, Myrthe aan de Stegge, Jos Hermans, Johan Teunis, Rinke J van Tatenhove-Pel, Bas Teusink, Herwig Bachmann, and Oscar P Kuipers. 2020. Enhancement of amino acid production and secretion by Lactococcus lactis using a droplet-based biosensing and selection system. Metabolic Engineering Communications 11 (2020), e00133.

[19] Csaba Horváth. 2013. High-performance liquid chromatography: advances and perspectives. (2013).

[20] Haiyan Hu, Qianyi Huang, and Qian Zhang. 2023. Babynutri: a cost-effective baby food macronutrients analyzer based on spectral reconstruction. Proceedings of the ACM on Interactive, Mobile, Wearable and Ubiquitous Technologies 7, 1 (2023), 1–30.

[21] Yongzhi Huang, Kaixin Chen, Yandao Huang, Lu Wang, and Kaishun Wu. 2021. Vi-liquid: unknown liquid identification with your smartphone vibration. In Proceedings of the 27th Annual International Conference on Mobile Computing and Networking. 174–187.

[22] Yongzhi Huang, Kaixin Chen, Lu Wang, Yinying Dong, Qianyi Huang, and Kaishun Wu. 2021. Lili: liquor quality monitoring based on light signals. In Proceedings of the 27th Annual International Conference on Mobile Computing and Networking. 256–268.

[23] Yu Liang Huang, Titus J Foellmer, Koon Chye Ang, Soo Beng Khoo, and Miranda GS Yap. 1995. Characterization and application of an on-line flow injection analysis/wall-jet electrode system for glucose monitoring during fermentation. Analytica chimica acta 317, 1-3 (1995), 223–232.

[24] Shinya Inoué and Charles J Koester. 1959. Optimum half-shade angle in polarizing instruments. Journal of the Optical Society of America 49, 6 (1959), 556–559.

[25] O Iupac. 1992. International union of pure and applied chemistry. Standard methods for the analysis of oils, fats and derivates (1992).

[26] Weiwei Jiang, Gabriele Marini, Niels van Berkel, Zhanna Sarsenbayeva, Zheyu Tan, Chu Luo, Xin He, Tilman Dingler, Jorge Goncalves, Yoshihiro Kawahara, et al. 2019. Probing sucrose contents in everyday drinks using miniaturized near-infrared spectroscopy scanners. Proceedings of the ACM on Interactive, Mobile, Wearable and Ubiquitous Technologies 3, 4 (2019), 1–25.

[27] Tanyawat Kaewsalud, Jessica Michelle Liony, Sitthidat Tongdonyod, Suphat Phongthai, and Wannaporn Klangpetch. 2025. Development of fructooligosaccharide-rich sugarcane juice by enzymatic method and enhancement of its microbial safety using high-pressure processing. Foods 14, 19 (2025), 3417.

[28] Masafumi Kameya and Yasuhisa Asano. 2014. Rapid enzymatic assays for L-citrulline and L-arginine based on the platform of pyrophosphate detection. Enzyme and microbial technology 57 (2014), 36–41.

[29] Andreas Kusterer, Christian Krause, Klaus Kaufmann, Matthias Arnold, and Dirk Weuster-Botz. 2008. Fully automated single-use stirred-tank bioreactors for parallel microbial cultivations. Bioprocess and biosystems engineering 31, 3 (2008), 207–215.

[30] Markus Lacorn and Thomas Hektor. 2025. Validation of Enzytec™ liquid D-glucose/D-fructose for enzymatic determination of D-glucose and D-fructose in selected foods and beverages: official method 2024.04 first action. Journal of AOAC International 108, 4 (2025), 572–594.

[31] Suman Lata and CS Pundir. 2013. L-amino acid biosensor based on L-amino acid oxidase immobilized onto NiHCNFe/c-MWCNT/PPy/GC electrode. International Journal of Biological Macromolecules 54 (2013), 250–257.

[32] Jiaxiu Li, Chunling Zhang, Hui Liu, Jiechao Liu, and Zhonggao Jiao. 2020. Profiles of sugar and organic acid of fruit juices: A comparative study and implication for authentication. Journal of Food Quality 2020, 1 (2020), 7236534.

[33] Tianxing Li, Derek Bai, Temiloluwa Prioleau, Nam Bui, Tam Vu, and Xia Zhou. 2020. Noninvasive glucose monitoring using polarized light.

In Proceedings of the 18th conference on embedded networked sensor systems. 544–557.

[34] Jingbo Liang, Dalong Zhang, Xuan Guo, Qingyang Xu, Xixian Xie, Chenglin Zhang, Gang Bai, Xue Xiao, and Ning Chen. 2013. At-line near-infrared spectroscopy for monitoring concentrations in temperature-triggered glutamate fermentation. Bioprocess and biosystems engineering 36, 12 (2013), 1879–1887.

[35] Yumeng Liang, Anfu Zhou, Huanhuan Zhang, Xinzhe Wen, and Huadong Ma. 2021. FG-LiquID: A contact-less fine-grained liquid identifier by pushing the limits of millimeter-wave sensing. Proceedings of the ACM on Interactive, Mobile, Wearable and Ubiquitous Technologies 5, 3 (2021), 1–27.

[36] Tianshu Liu and John P Sullivan. 2005. Pressure and temperature sensitive paints. Springer.

[37] Hidenori Matsui, Takahiro Hashizume, and Koji Yatani. 2018. Allight: An alcohol-sensing smart ice cube. Proceedings of the ACM on interactive, mobile, wearable and ubiquitous technologies 2, 3 (2018), 1–20.

[38] Shahrzad Mirzaei, Mariam Bebawy, Amr Mohamed Sharafeldin, and Mohamed Hefeeda. 2025. MobiLyzer: Fine-grained mobile liquid analyzer. Proceedings of the ACM on Interactive, Mobile, Wearable and Ubiquitous Technologies 9, 4 (2025), 1–37.

[39] Ani M Paloyan, Lusine H Melkonyan, and Gayane Ye Avetisova. 2022. Microbial approaches for amino acids production. In Microbial Syntrophy-Mediated Eco-enterprising. Elsevier, 177–208.

[40] Min Kyung Park and Young-Suk Kim. 2021. Mass spectrometry based metabolomics approach on the elucidation of volatile metabolites formation in fermented foods: A mini review. Food Science and Biotechnology 30, 7 (2021), 881–890.

[41] Johnnie Phuong, Billy Salgado, Jana Heiß, Ellen Steimers, Patrick Nickolaus, Lena Keller, Ulrich Fischer, Erik von Harbou, Daniel J Holland, Fabian Jirasek, et al. 2025. Real-time monitoring of fermentation processes in wine production with benchtop 1H NMR spectroscopy. Food Research International 203 (2025), 115741.

[42] Prasad L Polavarapu. 2002. Optical rotation: recent advances in determining the absolute configuration. Chirality 14, 10 (2002), 768–781.

[43] Tauhidur Rahman, Alexander T Adams, Perry Schein, Aadhar Jain, David Erickson, and Tanzeem Choudhury. 2016. Nutrilyzer: A mobile system for characterizing liquid food with photoacoustic effect. In Proceedings of the 14th ACM Conference on Embedded Networked Sensor Systems CD-ROM. 123–136.

[44] Meerza Abdul Razak and Buddolla Viswanath. 2015. Optimization of fermentation upstream parameters and immobilization of Corynebacterium glutamicum MH 20-22 B cells to enhance the production of L-lysine. 3 Biotech 5, 4 (2015), 531–540.

[45] Viviane Maria Rizelio, Laura Tenfen, Roberta da Silveira, Luciano Valdemiro Gonzaga, Ana Carolina Oliveira Costa, and Roseane Fett. 2012. Development of a fast capillary electrophoresis method for determination of carbohydrates in honey samples. Talanta 93 (2012), 62–66.

[46] Johannes Schiffels, Marcus EM Baumann, and Thorsten Selmer. 2011. Facile analysis of short-chain fatty acids as 4-nitrophenyl esters in complex anaerobic fermentation samples by high performance liquid chromatography. Journal of Chromatography A 1218, 34 (2011), 5848–5851.

[47] Fei Shang, Panlong Yang, Yubo Yan, and Xiang-Yang Li. 2022. LiqRay: Non-invasive and fine-grained liquid recognition system. In Proceedings of the 28th annual international conference on mobile computing and networking. 296–309.

[48] Fei Shang, Panlong Yang, Yubo Yan, and Xiang-Yang Li. 2023. PackquID: In-packet liquid identification using RF signals. Proceedings of the ACM on Interactive, Mobile, Wearable and Ubiquitous Technologies 6, 4 (2023), 1–27.

[49] Neha Sharma, Mariam Bebawy, Yik Yu Ng, and Mohamed Hefeeda. 2025. GlucoSense: Non-Invasive Glucose Monitoring using Mobile Devices. In Proceedings of the 31st Annual International Conference on Mobile Computing and Networking. 247–266.

[50] Neha Sharma, Muhammad Shahzaib Waseem, Shahrzad Mirzaei, and Mohamed Hefeeda. 2023. MobiSpectral: Hyperspectral imaging on mobile devices. In Proceedings of the 29th Annual International Conference on Mobile Computing and Networking. 1–15.

[51] Sakhamuri Sivakesava, Joseph Irudayaraj, and Demirci Ali. 2001. Simultaneous determination of multiple components in lactic acid fermentation using FT-MIR, NIR, and FT-Raman spectroscopic techniques. Process Biochemistry 37, 4 (2001), 371–378.

[52] Denghui Song, Anfu Zhou, Huadong Ma, and Jie Xiong. 2025. Molesen: From macro sensing to micro molecular-level taste sensing. In Proceedings of the 31st Annual International Conference on Mobile Computing and Networking. 17–32.

[53] Denghui Song, Anfu Zhou, Huadong Ma, and Jie Xiong. 2025. T-Oil: A Contactless Edible Oil Adulteration Perception Using Terahertz Signals. Proceedings of the ACM on Interactive, Mobile, Wearable and Ubiquitous Technologies 9, 2 (2025), 1–24.

[54] Tobias Steinwedel, Philipp Raithel, Jana Schellenberg, Carlotta Kortmann, Pia Gellermann, Mathias Belz, and Dörte Solle. 2024. Application of a Novel Disposable Flow Cell for Spectroscopic Bioprocess Monitoring. Chemosensors 12, 10 (2024), 202.

[55] Xue Sun, Wenwen Deng, Xudong Wei, Dingyi Fang, Baochun Li, and Xiaojiang Chen. 2023. Akte-liquid: Acoustic-based liquid identification with smartphones. ACM Transactions on Sensor Networks 19, 1 (2023), 1–24.

[56] Texas Instruments. 2015. OPT101 Monolithic Photodiode and Single-Supply Transimpedance Amplifier. Data Sheet, Rev. B. https://www.ti.com/lit/ds/symlink/opt101.pdf Document No. SBBS002B.

[57] Kento Tokuyama, Yoshiki Shimodaira, Yohei Kodama, Ryuzo Matsui, Yasuhiro Kusunose, Shunsuke Fukushima, Hiroaki Nakai, Yuichiro Tsuji, Yoshihiro Toya, Fumio Matsuda, et al. 2021. Soft-sensor development for monitoring the lysine fermentation process. Journal of bioscience and bioengineering 132, 2 (2021), 183–189.

[58] Valery V Tuchin. 2016. Polarized light interaction with tissues. Journal of biomedical optics 21, 7 (2016), 071114–071114.

[59] Franz Ulberth, Eric Aries, Oliver De Rudder, Georgios Kaklamanos, and Alain Maquet. 2024. Purity assessment of honey based on compound specific stable carbon isotope ratios obtained by LC-IRMS. Journal of AOAC International 107, 5 (2024), 884–887.

[60] Warren C Vosburgh. 1921. The Optical Rotation of Mixtures of Sucrose, Glucose and Fructose. Journal of the American Chemical Society 43, 2 (1921), 219–232.

[61] MJ Walker, S Cowen, K Gray, P Hancock, and DT Burns. 2022. Honey authenticity: the opacity of analytical reports-part 1 defining the problem. NPJ science of food 6, 1 (2022), 11.

[62] Bo Wang, Muhammad Shahzad, Xianglin Zhu, Khalil Ur Rehman, Muhammad Ashfaq, and Muhammad Abubakar. 2020. Soft-sensor modeling for l-lysine fermentation process based on hybrid ICS-MLSSVM. Scientific reports 10, 1 (2020), 11630.

[63] Ju Wang, Jie Xiong, Xiaojiang Chen, Hongbo Jiang, Rajesh Krishna Balan, and Dingyi Fang. 2017. TagScan: Simultaneous target imaging and material identification with commodity RFID devices. In Proceedings of the 23rd Annual International Conference on Mobile Computing and Networking. 288–300.

[64] Zhu Wang, Yifan Guo, Zhihui Ren, Wenchao Song, Zhuo Sun, Chao Chen, Bin Guo, and Zhiwen Yu. 2024. Liqdetector: Enabling container-independent liquid detection with mmwave signals based on a dual-reflection model. Proceedings of the ACM on Interactive, Mobile,

Wearable and Ubiquitous Technologies 7, 4 (2024), 1–24.

[65] Volker F Wendisch. 2014. Microbial production of amino acids and derived chemicals: synthetic biology approaches to strain development. Current opinion in biotechnology 30 (2014), 51–58.

[66] Kenneth B Wiberg, Yi-gui Wang, Michael J Murphy, and Patrick H Vaccaro. 2004. Temperature dependence of optical rotation: α-pinene, β-pinene pinane, camphene, camphor and fenchone. The Journal of Physical Chemistry A 108, 26 (2004), 5559–5563.

[67] Liming Wu, Bing Du, Yvan Vander Heyden, Lanzhen Chen, Liuwei Zhao, Miao Wang, and Xiaofeng Xue. 2017. Recent advancements in detecting sugar-based adulterants in honey–A challenge. TrAC Trends in Analytical Chemistry 86 (2017), 25–38.

[68] Qijun Wu and Xun Gong. 2015. A virtual instrument system for determining sugar degree of honey. Journal of Analytical Methods in Chemistry 2015, 1 (2015), 534795.

[69] Dongdong Xie, Yingqi Sun, and Yanan Lei. 2022. Effect of glucose levels on carbon flow rate, antioxidant status, and enzyme activity of yeast during fermentation. Journal of the Science of Food and Agriculture 102, 12 (2022), 5333–5347.

[70] Atsushi Yamamoto, Akinobu Matsunaga, Kazuichi Hayakawa, Eiichi Mizukami, and Motoichi Miyazaki. 1991. Polarized photometric detector for high-performance liquid chromatography. Analytical sciences 7, 5 (1991), 719–721.

[71] Atsushi Yokota and Masato Ikeda. 2017. Amino acid fermentation. Springer.

[72] Shichao Yue and Dina Katabi. 2019. Liquid testing with your smartphone. In Proceedings of the 17th annual international conference on mobile systems, applications, and services. 275–286.

[73] Li Zhou, Can Deng, Wen-Jing Cui, Zhong-Mei Liu, and Zhe-Min Zhou. 2016. Efficient L-alanine production by a thermo-regulated switch in Escherichia coli. Applied biochemistry and biotechnology 178, 2 (2016), 324–337.

[74] Robert Zimmerleiter, Julian Kager, Ramin Nikzad-Langerodi, Vladimir Berezhinskiy, Frank Westad, Christoph Herwig, and Markus Brandstetter. 2020. Probeless non-invasive near-infrared spectroscopic bioprocess monitoring using microspectrometer technology: Zimmerleiter R. et al. Analytical and Bioanalytical Chemistry 412, 9 (2020), 2103–2109.